Scilight

Thermal Science and Applications
https://www.sciltp.com/journals/tsa



Article

Check for updates

Thermal-Runaway Investigation for a Cylindrical $LiFePO_4$ Cell in Battery Energy Storage Systems (BESS): A Fully Coupled Electro-Chemo-Thermo-Mechanical (ECTM) Perspective

Menglang Xu, Yutong Chai * and Shunde Yin

Department of Civil and Environmental Engineering, University of Waterloo, Waterloo, ON N2L 3G1, Canada
* Correspondence: y5chai@uwaterloo.ca

How To Cite: Xu, M.; Chai, Y.; Yin, S. Thermal-Runaway Investigation for a Cylindrical $LiFePO_4$ Cell in Battery Energy Storage Systems (BESS): A Fully Coupled Electro-Chemo-Thermo-Mechanical (ECTM) Perspective. *Thermal Science and Applications* **2026**, *1*(4), 358–371. https://doi.org/10.53941/tsa.2026.100022

Received: 29 April 2026
Revised: 20 August 2026
Accepted: 27 October 2026
Published: 30 October 2026

Abstract: This study presents a reduced-order electro-chemo-thermo-mechanical (ECTM) model for an 18650-format $LiFePO_4$ (LFP)/graphite cell under normal charging. A one-dimensional Doyle–Fuller–Newman electrochemical model is coupled to a two-dimensional axisymmetric equivalent-continuum thermal–mechanical model. Three controlled cases are compared over the first 100 s of a 1C charge: (1) the COMSOL material-default positive-electrode equilibrium potential, (2) a literature-derived LFP equilibrium-potential function that represents the plateau thermodynamics without explicitly resolving a phase field, and (3) Case 2 with a phenomenological stress-feedback term. At 100 s, the terminal voltage is approximately 3.360 V in Case 1 and 3.368 V in Cases 2 and 3. The corresponding average volumetric heat-generation rates are approximately 2.83×10^3 and 3.05×10^3 W m^{-3}, and the average temperature rises are approximately 0.133 and 0.145 K. The maximum equivalent-continuum von Mises stresses are only about 0.21 and 0.23 kPa, respectively; these values are not interpreted as electrode- or particle-scale stress. Cases 2 and 3 are practically indistinguishable at the plotted resolution, so the feedback coefficient is treated only as an uncalibrated sensitivity parameter. The model is therefore a short-time operational framework demonstration, not a thermal-runaway or experimentally validated safety model.

Keywords: battery energy storage system; $LiFePO_4$ battery; electro-chemo-thermo-mechanical coupling; reduced-order model; phase-separation-informed equilibrium potential; cylindrical cell; operational charging

1. Introduction

Lithium-ion batteries (LIBs) support portable electronics, electric and hybrid electric vehicles (EVs and HEVs), and stationary battery energy storage systems (BESSs). At the system level, equivalent-circuit models (ECMs) are widely used in battery management systems (BMSs), whereas physics-based electrochemical and thermal models provide spatially resolved quantities that can inform battery thermal-management-system (BTMS) design and operating-envelope studies [1–4].

Operational multiphysics models and thermal-runaway models serve different but complementary purposes. The former predict voltage, heat generation, temperature, deformation, and stress during intended operation; the latter additionally require abuse triggers, internal short circuits, separator failure, SEI and electrolyte decomposition, gas generation, venting, and strongly exothermic reaction kinetics [5–16]. None of those abuse mechanisms is included here. Consequently, the present results cannot predict thermal-runaway onset,

Copyright: © 2026 by the authors. This is an open access article under the terms and conditions of the Creative Commons Attribution (CC BY) license (https://creativecommons.org/licenses/by/4.0/).
Publisher's Note: Scilight stays neutral with regard to jurisdictional claims in published maps and institutional affiliations.

propagation, or a safety margin; at most, a validated operational model could later provide initial conditions to a separate abuse model.

Reduced-order electrochemical–thermal and electro-chemo-mechanical formulations are attractive when repeated simulations are needed for design-space screening, control-oriented studies, or parameter sensitivity analysis [4,17–23]. Their benefit depends on transparent constitutive choices and on recognizing the information lost during homogenization. In particular, a cell-scale equivalent continuum cannot be interpreted as a resolved electrode coating, separator, binder, or particle microstructure.

LFP electrodes exhibit a flat voltage plateau and two-phase $LiFePO_4/FePO_4$ behavior over much of their stoichiometric range. Explicit phase-field models can resolve phase boundaries, coherency strain, and metastable dynamics [24–29]. A much cheaper alternative is to retain the DFN transport equations while replacing the positive-electrode equilibrium potential by a literature-derived LFP stoichiometry function. That substitution is "phase-separation-informed" only in the reduced thermodynamic sense: it reproduces plateau-shaped equilibrium behavior but does not solve a phase-field equation or track a moving phase boundary.

This work therefore asks a narrow, objective question: how sensitive are short-time coupled cell-scale outputs to the positive-electrode equilibrium-potential closure and to a reduced stress-feedback term? A 1.1 Ah, 18650-format LFP/graphite model is charged at 1C, meaning a current numerically equal to the nominal ampere-hour capacity (1.1 A here), for 100 s. The three cases use (1) the COMSOL material-default LFP equilibrium potential, (2) a published LFP equilibrium-potential function, and (3) the Case 2 function plus an uncalibrated phenomenological stress correction. The contribution is the controlled comparison and reproducible hybrid-dimensional implementation, not a claim of new phase-field theory, cell-specific validation, or thermal-runaway prediction.

2. Materials and Methods

2.1. Model Geometry, Cell Specification, and Assumptions

The computational domain represents an 18650-format LFP/graphite cell with an 18 mm outer diameter, 65 mm height, 3.3 V nominal voltage, and 1.1 Ah nominal capacity [30]. The electrochemical domain resolves the negative electrode (40 μm), separator (25 μm), and positive electrode (70 μm) in one through-thickness dimension. The thermal and mechanical domains use a two-dimensional axisymmetric cylinder with anisotropic effective properties. The wound layers, steel can, mandrel, current-collector foils, tabs, binder, and separator are not mechanically resolved. The electrolyte is represented by the COMSOL Li-ion liquid-electrolyte property functions with an initial salt concentration of 1.2 mol L^{-1}; a specific solvent blend was not calibrated to a target cell. Table 1 shows the cell specification and representation used in the simulations.

Table 1. Cell specification and representation used in the simulations.

Item	Model Specification	Status/Source
Cell format	18650 cylinder; 18 mm diameter × 65 mm height	Nominal format; [30]
Nominal electrical rating	3.3 V; 1.1 Ah; 1C = 1.1 A	Datasheet-level reference; [30]
Positive electrode	$LiFePO_4$; 70 μm porous coating	Model input
Negative electrode	Graphite; 40 μm porous coating	Model input
Separator	25 μm porous separator	Model input
Electrolyte	$LiPF_6$-based liquid-electrolyte property functions; $c_{e,0}$ = 1200 mol m^{-3}	COMSOL material functions; composition not target-cell calibrated
Tabs and current collectors	Electrical boundaries only; tab temperature not resolved	Declared limitation

2.2. Electrochemical Model

The electrochemical submodel was implemented with the Lithium-Ion Battery interface in COMSOL Multiphysics 6.3.0.290 and follows the Doyle–Fuller–Newman porous-electrode framework [4,17,31–33]. The one-dimensional cell domain includes solid-state diffusion in representative spherical particles, electrolyte species transport, electronic and ionic charge conservation, and Butler–Volmer interfacial kinetics. The negative-electrode equilibrium-potential and kinetic functions use the COMSOL graphite material description in all three cases.

Lithium transport in each representative spherical active-material particle was governed by Fick's second law [33]:

$$\frac{\partial c_s}{\partial t} = \frac{1}{r_p^2}\frac{\partial}{\partial r_p}\left(D_s r_p^2 \frac{\partial c_s}{\partial r_p}\right) \tag{1}$$

where c_s is the lithium concentration in the solid phase, D_s is the solid-state diffusion coefficient, and r_p is the radial coordinate inside the particle. Symmetry was imposed at the particle center, and the lithium flux at the particle surface was coupled to the interfacial reaction current density.

Lithium-ion transport in the electrolyte was described by the species conservation equation:

$$\varepsilon_e \frac{\partial c_e}{\partial t} = \nabla\cdot(D_e^{eff}\nabla c_e) + \frac{1 - t_+^0}{F} a_s j \tag{2}$$

where ε_e is the electrolyte volume fraction, c_e is the electrolyte lithium-ion concentration, D_e^{eff} is the effective electrolyte diffusion coefficient, t_+^0 is the transference number, a_s is the specific interfacial area, and j is the interfacial reaction-current density [33].

Charge conservation in the electronically conductive solid matrix of the electrodes was expressed as:

$$\nabla\cdot(\sigma_s^{eff}\nabla\phi_s) = -a_s j \tag{3}$$

where σ_s^{eff} is the effective electronic conductivity of the solid phase and ϕ_s is the solid-phase potential. Similarly, charge conservation in the electrolyte phase was written as:

$$\nabla\cdot(\kappa_e^{eff}\nabla\phi_e + \kappa_D^{eff}\nabla \ln c_e) = a_s j \tag{4}$$

where κ_e^{eff} is the effective ionic conductivity, κ_D^{eff} is the diffusional-conductivity term, and ϕ_e is the electrolyte potential [33].

The interfacial charge transfer reaction at both electrodes was described using Butler–Volmer kinetics:

$$\begin{gathered} j = i_0 \\ j = i_0\left[\exp\left(\frac{\alpha_a F\eta}{RT}\right) - \exp\left(-\frac{\alpha_c F\eta}{RT}\right)\right] \end{gathered} \tag{5}$$

where i_0 is the exchange current density, α_a and α_c are the anodic and cathodic charge transfer coefficients, R is the universal gas constant, T is temperature, and η is the reaction overpotential. The reaction overpotential was defined as:

$$\eta = \phi_s - \phi_e - U \tag{6}$$

where U is the equilibrium potential of the electrode material, defined as a function of stoichiometry and, where applicable, temperature. In the present model, the exchange current density was also treated as concentration-dependent to capture the variation in reaction kinetics with local lithium content.

All three cases use the same concentration-dependent kinetic functions, initial state, geometry, transport, thermal, mechanical, and solver settings; only the positive-electrode equilibrium-potential closure and, in Case 3, the stated phenomenological stress-feedback term change.

2.3. Reduced Phase-Separation-Informed LFP Thermodynamics

Case 2 does not explicitly simulate phase separation. It retains the single-particle DFN transport description and uses a stoichiometry-dependent positive-electrode equilibrium potential fitted in prior LFP/graphite modeling studies [34–37]. Thus, no order parameter, gradient-energy term, phase-boundary motion, nucleation, hysteresis, or metastable relaxation is solved. The term phase-separation-informed denotes only the use of a plateau-shaped equilibrium-potential closure motivated by LFP two-phase thermodynamics.

Let $\theta_p = c_{s,p}^{surf}/c_{s,p}^{max}$. The literature fit was used over the published LFP stoichiometric window $0.0229 \le \theta_p \le 0.9421$, with numerical clamping at the endpoints. No refitting to measured OCV data from the target 1.1 Ah cell was performed. At the reference temperature, the implemented function is:

$$\begin{aligned} U_{p,\mathrm{eq}}(\theta_p) = 3.4323 &- 0.8428 exp\left[-80.2493(1 - \theta_p)^{1.3198}\right] - 3.2474\times10^{-6} exp\left[20.2645(1 - \right. \\ &\left. \theta_p)^{3.8003}\right] + 3.2482\times10^{-6} exp\left[20.2646(1 - \theta_p)^{3.7995}\right] \text{ V} \end{aligned} \tag{7}$$

Temperature dependence was added as:

$$U_p(\theta_p,T) = U_{p,\mathrm{eq}}(\theta_p) + (T - T_{\mathrm{ref}})\left(\frac{\partial U_p}{\partial T}\right) \tag{8}$$

where the published LFP entropy-coefficient fit [37,38] was:

$$\frac{\partial U_p}{\partial T} = -0.35376\theta_p^8 + 1.3902\theta_p^7 - 2.2585\theta_p^6 + 1.9635\theta_p^5 - 0.98716\theta_p^4 + 0.28857\theta_p^3 \\ -0.046272\theta_p^2 + 0.0032158\theta_p - 1.9186\times10^{-5}\ \mathrm{V\,K^{-1}} \tag{9}$$

Case 1 uses the COMSOL material-default LFP equilibrium-potential function. Because the proprietary material function and the literature fit have different reference curves, their cell voltages need not coincide. The approximately 8 mV difference at 100 s is therefore reported as model-form sensitivity, not as experimental evidence of phase separation.

2.4. Thermal Model

The thermal submodel solves transient heat conduction in the two-dimensional axisymmetric equivalent cell domain [39–42]. The effective radial and axial conductivities are 0.20 and 5.1 W m^{-1} K^{-1}, respectively, and the effective density and heat capacity are 2358 kg m^{-3} and 805 J kg^{-1} K^{-1}. No fluid-flow equations are present, so velocity vectors and streamlines are undefined.

$$(\rho C_p)_{\mathrm{eff}}\frac{\partial T}{\partial t} = \nabla\cdot(\mathbf{k}_{\mathrm{eff}}\nabla T) + Q_{tot} \tag{10}$$

where T is temperature, $(\rho C_p)_{\mathrm{eff}}$ is the effective volumetric heat capacity, $\mathbf{k}_{\mathrm{eff}}$ is the effective thermal conductivity tensor, and Q_{tot} is the total volumetric heat-generation rate. For the present axisymmetric model, the conductivity tensor was written as:

$$\mathbf{k}_{\mathrm{eff}} = \begin{bmatrix} k_r & 0 \\ 0 & k_z \end{bmatrix} \tag{11}$$

where k_r and k_z are the effective radial and axial thermal conductivities, respectively. This anisotropic formulation reflects the strong directional difference in heat transport caused by the spiral-wound layered architecture of cylindrical cells [41,43].

The total electrochemical heat source follows the standard battery energy balance [40,42] and includes irreversible reaction, ohmic, and reversible entropic contributions as evaluated by the COMSOL electrochemical interface.

$$Q_{tot} = Q_{\mathrm{ohm}} + Q_{\mathrm{rxn}} + Q_{\mathrm{rev}} \tag{12}$$

The irreversible reaction heat was written as:

$$Q_{\mathrm{rxn}} = a_s j\eta \tag{13}$$

and the reversible entropic heat was expressed as:

$$Q_{\mathrm{rev}} = a_s jT\frac{\partial U}{\partial T} \tag{14}$$

where a_s is the specific interfacial area, j is the local interfacial reaction current density, η is the reaction overpotential, U is the equilibrium potential, and $\partial U/\partial T$ is the entropic coefficient [40,44–46]. In the present hybrid-dimensional implementation, however, these terms were not transferred separately to the two-dimensional thermal domain. Instead, the thermal model received an equivalent time-dependent volumetric heat source, $Q_{\mathrm{ec,avg}}$, obtained from the total heat generation predicted by the one-dimensional electrochemical model and transferred to the axisymmetric thermal domain in reduced form. This treatment preserves the dominant cell-scale heating effect while remaining computationally efficient for the coupled ECTM simulations.

Heat dissipation at the external cell boundaries was represented using a convective heat-flux condition:

$$-\mathbf{n}\cdot(\mathbf{k}_{\mathrm{eff}}\nabla T) = \mathrm{h}(T - T_\infty) \tag{15}$$

where $\mathbf{n}$ is the outward unit normal vector, h is the convective heat-transfer coefficient, and T_∞ is the ambient temperature. Along the symmetry axis of the axisymmetric domain, zero normal heat flux was imposed.

The thermal model is restricted to operational heat generation. It excludes SEI and electrolyte decomposition, gas generation, separator melting, internal short circuits, venting, combustion, and all other abuse-reaction kinetics. It therefore cannot be used to infer thermal-runaway onset or propagation.

2.5. Equivalent-Continuum Mechanical Model

The same axisymmetric domain was assigned a small-strain, quasi-static, isotropic linear-elastic constitutive law with an effective Young's modulus of 0.75 GPa and Poisson ratio of 0.30 [47]. These values originate from a graphite composite-electrode measurement and were transferred as cell-domain effective properties; they were not derived by homogenizing the cathode, separator, foils, can, and electrolyte, and were not calibrated to the target cell. Accordingly, the resulting stress is an equivalent-continuum sensitivity output rather than a resolved cell-can, coating, binder, separator, or particle stress.

Under quasi-static conditions, the local mechanical equilibrium of the cell was governed by:

$$\nabla \cdot \sigma + b = 0 \tag{16}$$

where σ is the Cauchy stress tensor and b is the body-force vector. Since gravitational and inertial effects are negligible compared with the stress generated by thermal and electrochemical expansion, b was neglected in the present model [18].

The total infinitesimal strain tensor was obtained from the displacement field u = (u_r, u_z). In the 2D axisymmetric representation, the nonzero strain components were written as:

$$\varepsilon_{rr} = \frac{\partial u_r}{\partial r}, \varepsilon_{zz} = \frac{\partial u_z}{\partial z}, \varepsilon_{\theta\theta} = \frac{u_r}{r}, \gamma_{rz} = \frac{\partial u_r}{\partial z} + \frac{\partial u_z}{\partial r} \tag{17}$$

where u_r and u_z are the radial and axial displacements, respectively. This formulation allows the model to capture radial expansion or contraction, axial deformation, and the resulting stress nonuniformity within the equivalent cylindrical cell domain [18].

The total strain was decomposed into elastic, thermal, and electrochemical-induced contributions:

$$\varepsilon = \varepsilon^e + \varepsilon^{\mathrm{th}} + \varepsilon^{\mathrm{ch}} \tag{18}$$

where ε^e is the recoverable elastic strain, $\varepsilon^{\mathrm{th}}$ is the thermal strain, and $\varepsilon^{\mathrm{ch}}$ is the chemical or lithiation-induced eigenstrain. The corresponding constitutive relation was written as:

$$\sigma = \mathbf{C}:(\varepsilon - \varepsilon^{\mathrm{th}} - \varepsilon^{\mathrm{ch}}) \tag{19}$$

The stiffness tensor was defined by the effective Young's modulus and Poisson ratio. This assignment is a major modeling uncertainty because constituent-level properties and contacts are not resolved [18,21,47].

The thermal strain and electrochemical-induced strain were defined as:

$$\varepsilon^{\mathrm{th}} = \alpha_{\mathrm{eff}}(T - T_{\mathrm{ref}})\mathbf{I} \tag{20}$$

where α_{eff} is the effective coefficient of thermal expansion, T_{ref} is the reference temperature, $\mathbf{I}$ is the identity tensor. Following the standard eigenstrain based treatment of lithiation-induced deformation in lithium-ion battery mechanics [48,49], the local concentration-dependent chemical strain was recast here in reduced cell-scale form using averaged electrode stoichiometric descriptors. Specifically, effective electrode-level chemical strains were defined as:

$$\varepsilon_n = \beta_n(\bar{\theta}_n - \bar{\theta}_{n,ref}), \varepsilon_p = \beta_p(\bar{\theta}_p - \bar{\theta}_{p,ref}) \tag{21}$$

where β_n and β_p are effective chemical expansion coefficients, and $\bar{\theta}_n$ and $\bar{\theta}_p$ are the averaged normalized lithiation states of the negative and positive electrodes, respectively. These two electrode contributions were then combined into a cell-scale equivalent chemical eigenstrain:

$$\varepsilon_{\mathrm{ch}} = w_n\varepsilon_n + w_p\varepsilon_p \tag{22}$$

where w_n and w_p are weighting factors associated with the effective negative- and positive electrode thickness contributions. In the solid-mechanics implementation, this equivalent $\varepsilon_{\mathrm{ch}}$ was applied as an isotropic external eigenstrain in the axisymmetric cell domain. For post-processing and for the subsequent coupling analysis, the hydrostatic-stress was monitored as the mechanically relevant scalar stress measure, since it provides a reduced descriptor for stress-dependent electrochemical feedback at the cell scale [49,50].

The mechanical formulation includes reversible thermal strain and a thickness-weighted chemical eigenstrain. It omits plasticity, fracture, binder damage, particle cracking, layer sliding, delamination, can contact, preload, irreversible swelling, and gas pressure. No measured swelling or strain data were used for calibration.

2.6. Electrochemical–Thermal–Mechanical Coupling and Case Definitions

The one-dimensional electrochemical model provides volume-averaged heat generation and electrode lithiation states to the axisymmetric thermal and mechanical domains. Temperature feeds back to the electrochemical material properties. The mechanical field receives the temperature and the equivalent chemical eigenstrain. This hybrid-dimensional exchange reduces computational cost but removes layer-resolved gradients.

Case 3 adds a reduced mechanics-to-electrochemistry term to Case 2. The positive-electrode potential becomes $U_p^3 = U_p^{eq}(\theta_p) + (T - T_{ref})(\partial U_p/\partial T) + k_\sigma \sigma_{fb}$, with $k_\sigma = 1 \times 10^{-5}$ V Pa^{-1}. Here σ_{fb} is the transferred reduced stress descriptor, not the local von Mises stress. The coefficient is an assumed phenomenological sensitivity parameter and is not derived from partial molar volume or fitted to experiment. Therefore, Case 3 tests numerical coupling sensitivity only; it is not a validated mechanics-modified thermodynamic model.

$$U_{p,mech}^{eq} = U_p(\theta_p) + (T - T_{ref})\frac{dU}{dT}(\theta_p) + k_{E,p}\sigma_{fb} \tag{23}$$

The model inputs are geometry, material and transport properties, initial stoichiometries and temperature, applied current, convection coefficient, and mechanical coefficients. Primary outputs are terminal voltage, electrochemical heat generation, average and spatial temperature, displacement, and equivalent-continuum stress. The controlled case definitions are summarized in Table 2.

Table 2. Controlled simulation cases.

Case	Positive-Electrode Equilibrium Potential	Mechanical Feedback	Interpretive Purpose
1: Baseline	COMSOL material-default LFP function	None	Reference implementation
2: Phase-informed	Literature LFP plateau function	None	OCP model-form sensitivity
3: Feedback	Same as Case 2	Phenomenological $k_\sigma \sigma_{fb}$ term	Numerical sensitivity of reduced feedback

2.7. Boundary and Initial Conditions

All cases use a 1.1 A galvanostatic charge for 0–100 s. The negative current collector is the electrical reference and the positive current collector receives the applied current. Electrolyte current and species flux are zero at the external current-collector boundaries. Particle-center symmetry and interfacial flux conditions close the particle problems. The cell starts at 298.15 K with $c_{e,0}$ = 1200 mol m^{-3}, negative- and positive-electrode stoichiometries of 0.55042 and 0.44791, respectively, and zero displacement/stress.

At the electronically conductive boundaries, the electrical boundary conditions were written as:

$$\phi_s = 0 \text{ on the negative current collector} \tag{24}$$

$$-\mathbf{n}\cdot\mathbf{i}_s = i_{app} \text{ on the positive current collector} \tag{25}$$

where ϕ_s is the solid-phase potential, $\mathbf{i}_s$ is the solid-phase current density vector, $\mathbf{n}$ is the outward unit normal vector, and i_{app} is the prescribed applied current density corresponding to 1C rate. At electrolyte boundaries adjacent to the current collectors, zero ionic current and zero salt flux were imposed:

$$\mathbf{n}\cdot\mathbf{i}_e = 0, \ \mathbf{n}\cdot\mathbf{N}_e = 0 \tag{26}$$

where $\mathbf{i}_e$ is the electrolyte current density vector and $\mathbf{N}_e$ is the electrolyte species flux. At the particle scale, symmetry was imposed at the particle center, whereas the lithium flux at the particle surface was determined by the local interfacial reaction rate defined in the porous electrode model.

The entire exposed axisymmetric outer boundary uses convection to T_∞ = 298.15 K with h = 10 W m^{-2} K^{-1}; the symmetry axis has zero normal heat flux. Because tabs are not explicit geometric domains, tab-specific heat generation and tab temperature are not predicted.

$$-\mathbf{n}\cdot(\mathbf{k}_{eff}\nabla T) = \mathrm{h}(T - T_\infty) \tag{27}$$

Axisymmetry imposes zero radial displacement on the centerline. One axial reference constraint removes rigid-body motion, while remaining exterior boundaries are traction free. No external clamping pressure or can contact is applied.

The initial conditions were prescribed from the reference operating state of the cell prior to the start of the simulated galvanostatic charging process. The temperature field was initialized uniformly as：

$$T(\mathbf{x},0) = T_0 \tag{28}$$

where T_0 is the initial cell temperature, usually taken equal to the ambient temperature unless preheating or precooling is considered. The initial electrolyte concentration was also spatially uniform:

$$c_e(\mathbf{x},0) = c_{e,0} \tag{29}$$

and the initial solid-phase lithium concentration in each electrode was assigned from the prescribed initial stoichiometry:

$$c_{s,i}(r_p,\mathbf{x},0) = \theta_{i,0} c_{s,i}^{\max} \quad (i = n,p) \tag{30}$$

where $c_{e,0}$ is the initial electrolyte concentration, $\theta_{I,0}$ is the initial stoichiometric fraction of electrode i, and $c_{s,i}^{\max}$ is the maximum solid-phase lithium concentration. The initial stoichiometries of the positive and negative electrodes were selected to be consistent with the prescribed initial state of charge of the full cell, which is the standard initialization approach in COMSOL lithium-ion battery models.

For the mechanical field, the initial displacement was taken as zero and the stress-free configuration was used as the reference state at $t = 0$, such that thermal strain and the reduced electrochemically induced eigenstrain developed only after the onset of current loading. This initialization is appropriate for the present operational model because the objective is to track the evolution of temperature rise, lithiation-induced deformation, and stress accumulation relative to the initial undeformed state. Other specific values and the initial electrode stoichiometries used in each simulation case are referred in Table A1.

2.8. Numerical Implementation, Unit Audit, and Assessment Scope

COMSOL Multiphysics 6.3.0.290 was used for physics setup, meshing, and solution. The electrochemical through-thickness domain uses one-dimensional edge elements with local maximum element sizes down to 4.99 μm in the electrode/separator region, and each spherical particle extra dimension uses 10 radial elements. The thermal–mechanical cell domain uses a free-triangular mesh with nominal element sizes from 19.5 μm to 4.36 mm. Electrochemical potentials and concentrations, temperature, and displacement use quadratic interpolation (serendipity quadratic for displacement). The transient system contains approximately 1399 degrees of freedom.

Time integration uses an adaptive backward-differentiation formula with maximum order 2 and relative tolerance 10^{-3}; results are stored every 0.2 s from 0 to 100 s. Nonlinear fields are solved in a fully coupled sequence with a maximum of four iterations per step and damping 0.9, with a PARDISO direct linear solver where selected. The reported 100 s interval is only 2.78% of an ideal 3600 s 1C charge. No full-cycle, mesh-independence, time-step convergence, or stability study was performed; this is stated explicitly rather than inferred from solver completion.

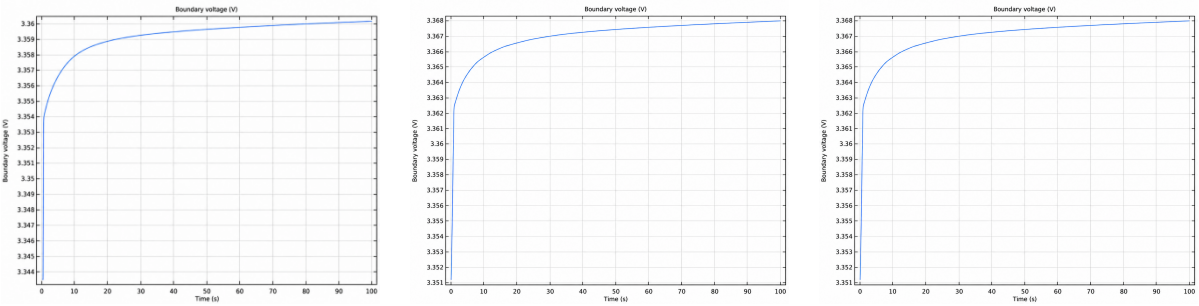
A dimensional audit confirmed that the transferred heat source is in W m^{-3} and that the thermal storage term uses ρCp with SI units. The small temperature rise is consistent with the short simulated duration and the imposed convection, but it has not been validated against calorimetry or thermocouple data. Likewise, the voltage was checked for smooth numerical behavior but not compared with a target-cell charge curve, and the mechanical output was not compared with swelling or strain measurements. The results below are therefore comparative model outputs, not quantitative experimental validation.

3. Results and Discussion

3.1. Terminal-Voltage Response

Figure 1 presents the three separately exported terminal-voltage histories. All results cover the same 1C, 100 s interval and are shown without constructing unsupplied difference curves.

Case 1 increases from approximately 3.343 to 3.360 V. Cases 2 and 3 begin near 3.351 V and end near 3.368 V; their curves are visually coincident. The approximately 8 mV offset relative to Case 1 is best interpreted as a difference between two positive-electrode equilibrium-potential reference curves. It is not proof that a phase boundary has been resolved, and without a measured target-cell OCV curve the more accurate closure cannot be identified. The negligible Case 2–Case 3 difference also shows that the chosen feedback term has no practical effect over this operating window.

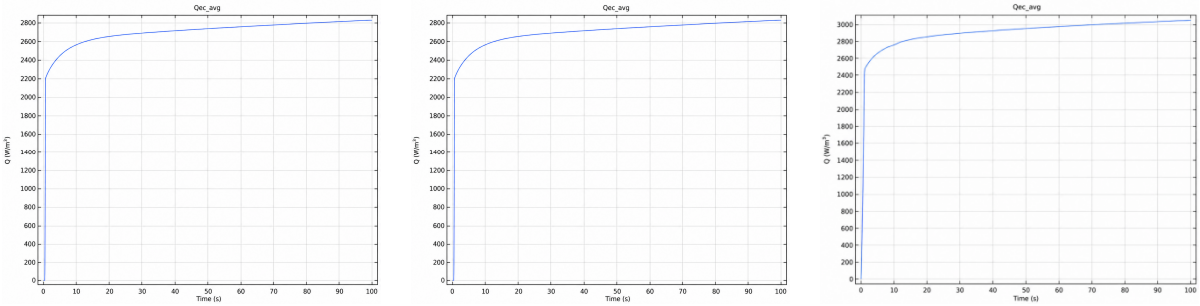


(**a**) Case 1: baseline (**b**) Case 2: phase-informed (**c**) Case 3: feedback

Figure 1. Terminal voltage during the first 100 s of 1C charging: (**a**) Case 1, COMSOL material-default positive-electrode equilibrium potential; (**b**) Case 2, literature LFP equilibrium potential; and (**c**) Case 3, Case 2 plus phenomenological stress feedback.

3.2. Heat Generation and Average Temperature Rise

The average electrochemical heat-generation histories are compared in Figure 2. Values are reported in W m^{-3}, consistent with the thermal-source interface and the SI-unit audit described in Section 2.8.

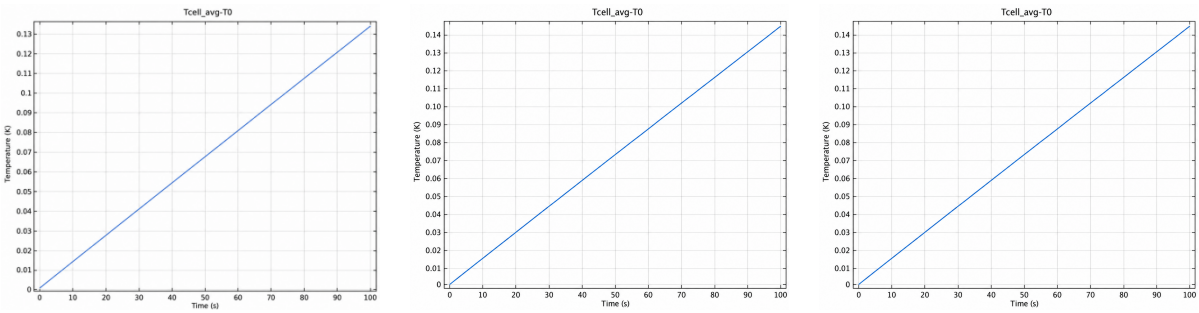


(**a**) Case 1: baseline (**b**) Case 2: phase-informed (**c**) Case 3: feedback

Figure 2. Volume-averaged electrochemical heat-generation rate for the three cases during the first 100 s of 1C charging.

After the initial transient, Case 1 rises from about 2.2 × 10^3 to 2.83 × 10^3 W m^{-3}, whereas Cases 2 and 3 end near 3.05 × 10^3 W m^{-3}. The roughly 0.22 × 10^3 W m^{-3} end-point difference is consistent with the changed equilibrium potential and associated overpotential/entropic terms. Because all transport and boundary parameters are fixed, this difference is a constitutive-model sensitivity, not an independently validated increase in physical heat release.

The average temperature rise is approximately 0.133 K in Case 1 and 0.145 K in Cases 2 and 3 at 100 s, a difference of only about 0.012 K (Figure 3). This small response follows from the short 100 s window, the modest volumetric source, the effective thermal mass, and convection on the cell surface. It is unrelated to thermal runaway: no accelerating temperature rate, decomposition heat, venting, or internal short circuit is modeled. A full 3600 s charge and target-cell temperature data are needed before drawing conclusions about mature gradients or BTMS performance.

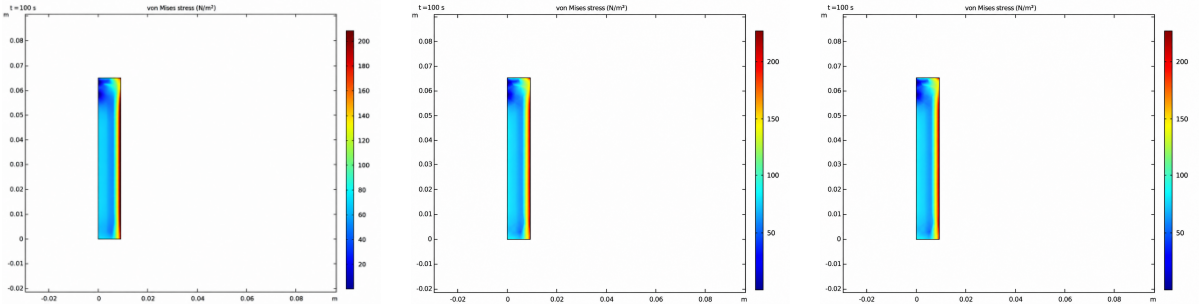


(**a**) Case 1: baseline (**b**) Case 2: phase-informed (**c**) Case 3: feedback

Figure 3. Volume-averaged temperature rise for the three cases during the first 100 s of 1C charging.

3.3. Equivalent-Continuum Mechanical Response

The plotted maxima are approximately 0.21 kPa for Case 1 and 0.23 kPa for Cases 2 and 3. These values are orders of magnitude below MPa-scale coating, particle, can, or constrained-cell stresses commonly reported in experiments and detailed models. The discrepancy is not presented as a physically validated stress prediction. It follows from assigning a single compliant modulus to a traction-free equivalent continuum, applying a reduced average eigenstrain, omitting contacts and layer mismatch, and considering only 100 s of charging. Figure 4 can therefore support only the narrow observation that the implemented equivalent-continuum output changes slightly when the upstream OCP closure changes.



(**a**) Case 1: baseline (**b**) Case 2: phase-informed (**c**) Case 3: feedback

Figure 4. Equivalent-continuum von Mises stress at t = 100 s. The supplied Case 3 export is pixel-identical to the Case 2 panel at the available resolution.

3.4. Coupled Interpretation and Limitations

Across the supplied outputs, the main model-form effect is introduced by the literature LFP equilibrium potential: relative to Case 1, it shifts voltage by about 8 mV at 100 s, heat generation by about 0.22×10^3 W m^{-3}, average temperature by about 0.012 K, and the equivalent-continuum stress by about 0.02 kPa. The direction is consistent along the coupling chain—electrode thermodynamics modifies overpotential and heat generation, which slightly modifies temperature and the reduced eigenstrain response. However, the magnitudes are too small and the evidence too limited to establish predictive superiority.

Case 3 adds no visually resolvable improvement relative to Case 2. Its present practical value is therefore limited to demonstrating that a feedback channel can be implemented numerically. A physically meaningful feedback model would require a thermodynamically derived stress–chemical-potential relation, resolved or well-homogenized stresses, and calibration against voltage and deformation data over a wider SOC range.

The principal limitations are: no explicit phase-field physics or hysteresis; no target-cell OCV, voltage, temperature, swelling, or strain validation; no mesh or time-step independence study; no full-charge or multi-rate analysis; no resolved tabs, can, layers, contacts, or constituent mechanics; and no aging, plating, SEI, gas, internal-short, or abuse chemistry. These omissions are compatible with a preliminary operational framework study but preclude thermal-runaway, BESS-safety, or mechanical-integrity claims.

4. Conclusions

A hybrid 1D electrochemical–2D axisymmetric thermal–mechanical model was used to compare three constitutive closures during the first 100 s of a 1C charge. Replacing the COMSOL material-default LFP equilibrium potential with a literature plateau function changed the 100 s terminal voltage from approximately 3.360 to 3.368 V, the average heat-generation rate from 2.83×10^3 to 3.05×10^3 W m^{-3}, and the average temperature rise from 0.133 to 0.145 K.

The predicted equivalent-continuum stress changed from approximately 0.21 to 0.23 kPa, but this magnitude is not physically representative of resolved cell or electrode stress. Adding the phenomenological mechanical feedback term produced no visible difference from the phase-informed case at the plotted resolution.

Accordingly, the study demonstrates model-form sensitivity and a computational coupling workflow under normal operation; it does not validate an explicit phase-separation model or predict thermal runaway. Experimental calibration, mesh/time-step studies, wider SOC and C-rate ranges, full-cycle simulations, and constituent-resolved mechanics are required before predictive or safety use.

Author Contributions

M.X. and Y.C.: writing—original draft preparation; S.Y.: supervision. All authors have read and agreed to the published version of the manuscript.

Funding

This research received no external funding.

Data Availability Statement

Data will be made available on request.

Conflicts of Interest

The authors declare no conflict of interest. Given the role as Editorial Board member, Shunde Yin had no involvement in the peer review of this paper and had no access to information regarding its peer-review process. Full responsibility for the editorial process of this paper was delegated to another editor of the journal.

Use of AI and AI-Assisted Technologies

No AI tools were utilized for this paper.

Nomenclature

Abbreviations used in this work

Abbreviation	Definition
BESS	battery energy storage system
BMS	battery management system
BTMS	battery thermal-management system
DFN	Doyle–Fuller–Newman
ECM	equivalent-circuit model
ECTM	electro-chemo-thermo-mechanical
EV	electric vehicle
HEV	hybrid electric vehicle
LFP	lithium iron phosphate
LIB	lithium-ion battery
OCP/OCV	open-circuit potential/open-circuit voltage
SEI	solid–electrolyte interphase
SOC	state of charge
TR	thermal runaway

Principal Roman symbols

Symbol	Meaning	Unit
c_e	electrolyte lithium-ion concentration	mol m^{-3}
c_s	solid-phase lithium concentration	mol m^{-3}
D_e, D_s	electrolyte and solid diffusion coefficients	m^2 s^{-1}
E	effective Young's modulus	Pa
F	Faraday constant	C mol^{-1}
h	convective heat-transfer coefficient	W m^{-2} K^{-1}
i_0	exchange-current density	A m^{-2}
j	interfacial reaction current density	A m^{-2}
k_r, k_z	radial and axial thermal conductivities	W m^{-1} K^{-1}
$\dot{Q}$	volumetric heat-generation rate	W m^{-3}
R	universal gas constant	J mol^{-1} K^{-1}
T	temperature	K
U	equilibrium potential	V
u	displacement	m

Greek symbols

Symbol	Meaning	Unit
α	thermal-expansion coefficient	K^{-1}
ε	strain or phase volume fraction, as identified by context	—
η	reaction overpotential	V
κ	effective ionic conductivity	S m^{-1}
ν	Poisson ratio	—
ρ	effective density	kg m^{-3}
σ	Cauchy stress tensor	Pa
σ_s	effective electronic conductivity	S m^{-1}
ϕ_e, ϕ_s	electrolyte and solid electric potentials	V

θ	electrode stoichiometry	—

Subscripts and superscripts

Notation	Meaning
0	initial or reference value
avg	volume average
eff	effective property
e	electrolyte phase
fb	feedback descriptor
max	maximum value
n	negative electrode
p	positive electrode
ref	reference state
s	solid phase
surf	particle-surface value
th, ch	thermal and chemical contributions

Appendix A. Model Parameters and Provenance

Table A1. Principal parameters used in the COMSOL model. "Model input" denotes a value read from the supplied .mph file; it does not imply calibration to the target cell.

Symbol	Description	Value	Unit	Provenance
Rcell	Cell outer radius	9	mm	model input; [30]
Hcell	Cell height	65	mm	model input; [30]
Qnom	Nominal capacity	1.1	Ah	model input; [30]
I1C	Applied 1C current	1.1	A	From Qnom
Ljr	Equivalent jelly-roll length	1.2	m	Model input
Ln/Lsep/Lp	Negative/separator/positive thickness	40/25/70	μm	Model input; literature-informed
εs,n/εs,p	Active-material volume fractions	0.56/0.43	—	Model input
εe,n/εe,p/εe,sep	Electrolyte volume fractions	0.40/0.40/0.54	—	Model input
Rp,n/Rp,p	Particle radii	3.5/1.0	μm	Model input
Ds,n/Ds,p	Solid diffusion coefficients	2×10^{-14}/1×10^{-15}	$m^2\ s^{-1}$	Model input; [4,17]
cs,max,n/cs,max,p	Maximum solid concentrations	31/23	kmol m^{-3}	Model input
i0,n/i0,p	Exchange-current densities	6.5/1.8	A m^{-2}	Model input
ce,0	Initial electrolyte concentration	1200	mol m^{-3}	Model input
t+	Li-ion transference number	0.46	—	Model input
σs,n/σs,p	Solid-phase conductivities	100/10	S m^{-1}	Model input
θn,0/θp,0	Initial electrode stoichiometries	0.55042/0.44791	—	Model input
T0/Tref/T∞	Initial/reference/ambient temperature	298.15	K	Model input
h	External convection coefficient	10	W m^{-2} K^{-1}	Model input; assumed
kr/kz	Effective radial/axial conductivity	0.20/5.1	W m^{-1} K^{-1}	Model input; [41,51]
ρeff	Effective density	2358	kg m^{-3}	Model input
Cp,eff	Effective heat capacity	805	J kg^{-1} K^{-1}	Model input; [51]
Eeff	Equivalent-continuum Young's modulus	0.75	GPa	Transferred graphite-composite value; [47]
νeff	Equivalent-continuum Poisson ratio	0.30	—	Transferred graphite-composite value; [47]
αeff	Effective thermal-expansion coefficient	2.0×10^{-5}	K^{-1}	Model input; literature-assigned [52]
$\bar{V}$n/$\bar{V}$p	Partial molar volumes	4.17×10^{-6}/ 3.0×10^{-6}	$m^3\ mol^{-1}$	Model input; [47,53]
kDs,n/kDs,p	Stress sensitivities of solid diffusivity	5×10^{-3}/5×10^{-3}	Pa^{-1}	Model input; uncalibrated
kσ	Stress-feedback coefficient	1×10^{-5}	V Pa^{-1}	Assumed sensitivity; uncalibrated
Output interval	Stored solution interval	0.2	s	Model input
Relative tolerance	Transient solver tolerance	1×10^{-3}	—	Model input

References

1. Kim, T.; Song, W.; Son, D.Y.; et al. Lithium-ion batteries: Outlook on present, future, and hybridized technologies. *J. Mater. Chem. A* **2019**, *7*, 2942–2964. https://doi.org/10.1039/c8ta10513h.
2. Chen, T.; Li, M.; Bae, J. Recent Advances in Lithium Iron Phosphate Battery Technology: A Comprehensive Review. *Batteries* **2024**, *10*, 424. https://doi.org/10.3390/batteries10120424.
3. Gao, Z.W.; Lan, T.; Yin, H.; et al. Development and Commercial Application of Lithium-Ion Batteries in Electric Vehicles: A Review. *Processes* **2025**, *13*, 756. https://doi.org/10.3390/pr13030756.
4. Prada, E.; Di Domenico, D.; Creff, Y.; et al. A Simplified Electrochemical and Thermal Aging Model of $LiFePO_4$-Graphite Li-ion Batteries: Power and Capacity Fade Simulations. *J. Electrochem. Soc.* **2013**, *160*, A616–A628. https://doi.org/10.1149/2.053304jes.
5. Wang, Q.; Ping, P.; Zhao, X.; et al. Thermal runaway caused fire and explosion of lithium ion battery. *J. Power Sources* **2012**, *208*, 210–224. https://doi.org/10.1016/j.jpowsour.2012.02.038.
6. Feng, X.; Ouyang, M.; Liu, X.; et al. Thermal runaway mechanism of lithium ion battery for electric vehicles: A review. *Energy Storage Mater.* **2018**, *10*, 246–267. https://doi.org/10.1016/j.ensm.2017.05.013.
7. Ramasubramanian, B.; Sundarrajan, S.; Chellappan, V.; et al. Recent Development in Carbon-$LiFePO_4$ Cathodes for Lithium-Ion Batteries: A Mini Review. *Batteries* **2022**, *8*, 133. https://doi.org/10.3390/batteries8100133.
8. Finegan, D.P.; Darcy, E.; Keyser, M.; et al. Characterising thermal runaway within lithium-ion cells by inducing and monitoring internal short circuits. *Energy Environ. Sci.* **2017**, *10*, 1377–1388. https://doi.org/10.1039/c7ee00385d.
9. Ren, D.; Feng, X.; Lu, L.; et al. An electrochemical-thermal coupled overcharge-to-thermal-runaway model for lithium ion battery. *J. Power Sources* **2017**, *364*, 328–340. https://doi.org/10.1016/j.jpowsour.2017.08.035.
10. Bugryniec, P.J.; Davidson, J.N.; Cumming, D.J.; et al. Pursuing safer batteries: Thermal abuse of $LiFePO_4$ cells. *J. Power Sources* **2019**, *414*, 557–568. https://doi.org/10.1016/j.jpowsour.2019.01.013.
11. Cannarella, J.; Arnold, C.B. Stress evolution and capacity fade in constrained lithium-ion pouch cells. *J. Power Sources* **2014**, *245*, 745–751. https://doi.org/10.1016/j.jpowsour.2013.06.165.
12. Rieger, B.; Erhard, S.V.; Rumpf, K.; et al. A New Method to Model the Thickness Change of a Commercial Pouch Cell during Discharge. *J. Electrochem. Soc.* **2016**, *163*, A1566–A1575. https://doi.org/10.1149/2.0441608jes.
13. Chen, H.; Xu, Y.; Wu, Y.; et al. External pressure effects on thermal runaway in prismatic $LiFePO_4$ batteries: Mechanistic insights for safer battery systems in electric vehicles. *eTransportation* **2025**, *26*, 100488. https://doi.org/10.1016/j.etran.2025.100488.
14. Jia, Z.; Song, L.; Mei, W.; et al. The preload force effect on the thermal runaway and venting behaviors of large-format prismatic $LiFePO_4$ batteries. *Appl. Energy* **2022**, *327*, 120100. https://doi.org/10.1016/j.apenergy.2022.120100.
15. Hahn, A.; Doose, S.; Saathoff, D.; et al. Effect of External Compression on the Thermal Runaway of Lithium-Ion Battery Cells during Crush Tests: Insights for Improved Safety Assessment. *Batteries* **2023**, *9*, 404. https://doi.org/10.3390/batteries9080404.
16. Battery Design. LFP Cell Clamping Pressure. Available online: https://www.batterydesign.net/lfp-cell-clamping-pressure (accessed on 18 February 2026).
17. Sarmadian, A.; Widanage, W.D.; Shollock, B.; et al. Experimentally-verified thermal-electrochemical simulations of a cylindrical battery using physics-based, simplified and generalised lumped models. *J. Energy Storage* **2023**, *70*, 107910. https://doi.org/10.1016/j.est.2023.107910.
18. Ai, W.; Kraft, L.; Sturm, J.; et al. Electrochemical Thermal-Mechanical Modelling of Stress Inhomogeneity in Lithium-Ion Pouch Cells. *J. Electrochem. Soc.* **2020**, *167*, 013512. https://doi.org/10.1149/2.0122001jes.
19. Al-Emrani, R.; Larsson, C.; Dahlberg, C.; et al. Electro-chemo-mechanical coupling in structural lithium-ion batteries: Experimental findings and numerical modelling. *Compos. Part B Eng.* **2026**, *311*, 113286. https://doi.org/10.1016/j.compositesb.2025.113286.
20. Carlstedt, D.; Runesson, K.; Larsson, F.; et al. On the coupled thermo–electro–chemo–mechanical performance of structural batteries with emphasis on thermal effects. *Eur. J. Mech.-A/Solids* **2022**, *94*, 104586. https://doi.org/10.1016/j.euromechsol.2022.104586.
21. Jung, T.; Song, Y.; Valentino, G.M.; et al. Mechanics-modified equilibrium potential for linear-elastic electrode materials. *EES Batter.* **2025**, *1*, 450–467. https://doi.org/10.1039/d5eb00045a.
22. Bucci, G.; Swamy, T.; Bishop, S.; et al. The Effect of Stress on Battery-Electrode Capacity. *J. Electrochem. Soc.* **2017**, *164*, A645–A654. https://doi.org/10.1149/2.0371704jes.
23. Schmider, D.; Bessler, W.G. Thermo-Electro-Mechanical Modeling and Experimental Validation of Thickness Change of a Lithium-Ion Pouch Cell with Blend Positive Electrode. *Batteries* **2023**, *9*, 354. https://doi.org/10.3390/batteries9070354.
24. Wu, L.; De Andrade, V.; Xiao, X.; et al. Phase Field Modeling of Coupled Phase Separation and Diffusion-Induced Stress in Lithium Iron Phosphate Particles Reconstructed from Synchrotron Nano X-ray Tomography. *J. Electrochem. Energy Convers. Storage* **2019**, *16*, 041006. https://doi.org/10.1115/1.4043155.

25. Cogswell, D.A.; Bazant, M.Z. Coherency Strain and the Kinetics of Phase Separation in $LiFePO_4$ Nanoparticles. *ACS Nano* **2012**, *6*, 2215–2225. https://doi.org/10.1021/nn204177u.
26. Bai, P.; Cogswell, D.A.; Bazant, M.Z. Suppression of Phase Separation in $LiFePO_4$ Nanoparticles during Battery Discharge. *Nano Lett.* **2011**, *11*, 4890–4896. https://doi.org/10.1021/nl202764f.
27. Zelič, K.; Katrašnik, T. Thermodynamically consistent derivation of chemical potential of a battery solid particle from the regular solution theory applied to $LiFePO_4$. *Sci. Rep.* **2019**, *9*, 2123. https://doi.org/10.1038/s41598-019-38635-2.
28. Wang, Q.; Zhang, G.; Li, Y.; et al. Application of phase-field method in rechargeable batteries. *npj Comput. Mater.* **2020**, *6*, 176. https://doi.org/10.1038/s41524-020-00445-w.
29. Weng, C.; Sun, J.; Peng, H. A unified open-circuit-voltage model of lithium-ion batteries for state-of-charge estimation and state-of-health monitoring. *J. Power Sources* **2014**, *258*, 228–237. https://doi.org/10.1016/j.jpowsour.2014.02.026.
30. APR18650M1B. 18650 Lithium Ion Power Cell. Available online: https://a123batteries.com/product_images/uploaded_images/APR18650M1B.pdf (accessed on 20 February 2026).
31. Lain, M.J.; Brandon, J.; Kendrick, E. Design Strategies for High Power vs. High Energy Lithium Ion Cells. *Batteries* **2019**, *5*, 64. https://doi.org/10.3390/batteries5040064.
32. COMSOL. Thermal Modeling of a Cylindrical Lithium-Ion Battery in 2D. COMSOL Application Library Documentation, Version 6.3. 2024. Available online: https://www.comsol.com/model/thermal-modeling-of-a-cylindrical-lithium-ion-battery-in-2d-10221 (accessed on 20 October 2026).
33. Doyle, M.; Fuller, T.F.; Newman, J. Modeling of Galvanostatic Charge and Discharge of the Lithium/Polymer/Insertion Cell. *J. Electrochem. Soc.* **1993**, *140*, 1526–1533. https://doi.org/10.1149/1.2221597.
34. Sarkar, S.; Amin, M.T.; El-Halwagi, M.M.; et al. Thermal behavior of $LiFePO_4$ battery at faster C-rates and lower ambient temperatures. *Process Saf. Environ. Prot.* **2024**, *186*, 118–133. https://doi.org/10.1016/j.psep.2024.03.095.
35. Renganathan, S.; Sikha, G.; Santhanagopalan, S.; et al. Theoretical Analysis of Stresses in a Lithium Ion Cell. *J. Electrochem. Soc.* **2010**, *157*, A155–A163. https://doi.org/10.1149/1.3261809.
36. Mohtat, P.; Nezampasandarbabi, F.; Mohan, S.; et al. On identifying the aging mechanisms in Li-ion batteries using two points measurements. In Proceedings of the 2017 American Control Conference (ACC), Seattle, WA, USA, 24–26 May 2017; pp. 98–103. https://doi.org/10.23919/acc.2017.7962937.
37. Chiew, J.; Chin, C.S.; Toh, W.D.; et al. A pseudo three-dimensional electrochemical-thermal model of a cylindrical $LiFePO_4$/graphite battery. *Appl. Therm. Eng.* **2019**, *147*, 450–463. https://doi.org/10.1016/j.applthermaleng.2018.10.108.
38. Viswanathan, V.V.; Choi, D.; Wang, D.; et al. Effect of entropy change of lithium intercalation in cathodes and anodes on Li-ion battery thermal management. *J. Power Sources* **2010**, *195*, 3720–3729. https://doi.org/10.1016/j.jpowsour.2009.11.103.
39. Jalkanen, K.; Aho, T.; Vuorilehto, K. Entropy change effects on the thermal behavior of a $LiFePO_4$/graphite lithium-ion cell at different states of charge. *J. Power Sources* **2013**, *243*, 354–360. https://doi.org/10.1016/j.jpowsour.2013.05.199.
40. Bernardi, D.; Pawlikowski, E.; Newman, J. A General Energy Balance for Battery Systems. *J. Electrochem. Soc.* **1985**, *132*, 5–12. https://doi.org/10.1149/1.2113792.
41. Drake, S.J.; Wetz, D.A.; Ostanek, J.K.; et al. Measurement of anisotropic thermophysical properties of cylindrical Li-ion cells. *J. Power Sources* **2014**, *252*, 298–304. https://doi.org/10.1016/j.jpowsour.2013.11.107.
42. Fuller, T.F.; Doyle, M.; Newman, J. Simulation and Optimization of the Dual Lithium Ion Insertion Cell. *J. Electrochem. Soc.* **1994**, *141*, 1–10. https://doi.org/10.1149/1.2054684.
43. Mattia, L.; Beiranvand, H.; Zamboni, W.; et al. Lithium-ion battery thermal modelling and characterisation: A comprehensive review. *J. Energy Storage* **2025**, *129*, 117114. https://doi.org/10.1016/j.est.2025.117114.
44. Bedürftig, B.; Oldenburger, M.; Hüfner, T.; et al. Measuring the reversible heat of lithium-ion cells via current pulses for modeling of temperature dynamics. *J. Power Sources* **2021**, *506*, 230110. https://doi.org/10.1016/j.jpowsour.2021.230110.
45. Clerici, D.; Martelli, S.; Mocera, F.; et al. Mechanical characterization of lithium-ion batteries with different chemistries and formats. *J. Energy Storage* **2024**, *84*, 110899. https://doi.org/10.1016/j.est.2024.110899.
46. Clerici, D.; Mocera, F.; Somà, A.; et al. Experimental Characterization of Lithium-Ion Cell Strain Using Laser Sensors. *Energies* **2021**, *14*, 6281. https://doi.org/10.3390/en14196281.
47. Liu, H.; Zhang, G.; Li, D.; et al. An Improved Experiment for Measuring Lithium Concentration-Dependent Material Properties of Graphite Composite Electrodes. *Nanomaterials* **2022**, *12*, 4448. https://doi.org/10.3390/nano12244448.
48. Krause, T.; Nusko, D.; Pitta Bauermann, L.; et al. Methods for Quantifying Expansion in Lithium-Ion Battery Cells Resulting from Cycling: A Review. *Energies* **2024**, *17*, 1566. https://doi.org/10.3390/en17071566.
49. Ipers, G.; Jiao, J.; Pathak, S.; et al. Rapid Simulation of Electro-Chemo-Mechanical Deformation of Li-ion Batteries Based on Porous Electrode Theory. *J. Electrochem. Soc.* **2024**, *171*, 050557. https://doi.org/10.1149/1945-7111/ad4f1e.
50. Uzun, F. Insights into Chemo-Mechanical Yielding and Eigenstrains in Lithium-Ion Battery Degradation. *Batteries* **2025**, *11*, 465. https://doi.org/10.3390/batteries11120465.

51. Spinner, N.S.; Hinnant, K.M.; Mazurick, R.; et al. Novel 18650 lithium-ion battery surrogate cell design with anisotropic thermophysical properties for studying failure events. *J. Power Sources* **2016**, *312*, 1–11. https://doi.org/10.1016/j.jpowsour.2016.01.107.
52. Kanagaraj, A.B.; Chaturvedi, P.; Alkindi, T.S.; et al. Mechanical, thermal and electrical properties of $LiFePO_4$/MWCNTs composite electrodes. *Mater. Lett.* **2018**, *230*, 57–60. https://doi.org/10.1016/j.matlet.2018.07.068.
53. Hofmann, T.; Westhoff, D.; Feinauer, J.; et al. Electro-chemo-mechanical simulation for lithium ion batteries across the scales. *Int. J. Solids Struct.* **2020**, *184*, 24–39. https://doi.org/10.1016/j.ijsolstr.2019.05.002.